PHYSICAL REVIEW C VOLUME 38, NUMBER 5 NOVEMBER 1988

Elastic scattering of protons by ^{16}O, ^{40}Ca, and ^{208}Pb at 200, 500, and 800 MeV: Relativistic and nonrelativistic analyses based on the impulse approximation

N. Ottenstein and S. J. Wallace
Department of Physics and Astronomy, University of Maryland, College Park, Maryland 20742

J. A. Tjon
Institute of Theoretical Physics, University of Utrecht, 3508 TA Utrecht, The Netherlands

(Received 3 December 1987)

Systematics of Dirac impulse approximation predictions for cross sections and spin observables in elastic proton scattering by ^{16}O, ^{40}Ca, and ^{208}Pb at energies of 200, 500, and 800 MeV are presented. The analysis is based on an optical potential constructed from complete sets of Lorentz-invariant *NN* amplitudes. The *NN* amplitudes are determined from a relativistic meson exchange model of the nuclear force. Comparisons are made with the original form of the Dirac impulse approximation, which is based on five Fermi terms to represent the *NN* interaction, and with the Schrödinger form of the impulse approximation. For the Dirac analyses, there is implicit coupling to virtual nucleon-antinucleon states. In order to illustrate these contributions, the Dirac equation is recast in the form of the Schrödinger equation and the resulting Schrödinger potentials are separated into "no-pair" and virtual-pair parts. The resulting virtual-pair part of the central potential is typically 25 MeV at the center of the nucleus for 200–800 MeV protons. A reasonable description of the experimental data is obtained over a broad energy range and over a wide variation of nuclear size when the analysis is based on complete sets of Lorentz-invariant amplitudes.

I. INTRODUCTION

Over the past few years, a dynamical basis for the Dirac optical potential has been developed using a relativistic description of nucleon-nucleon (*NN*) scattering based on meson-exchange dynamics.[1-3] Complete sets of Lorentz-invariant nucleon-nucleon (*NN*) amplitudes[4,5] are combined with the relativistic nuclear density to predict the Dirac optical potential using the impluse approximation. The generalized impulse approximation[3] based on the meson-exchange description of the nuclear force is denoted as IA2 herein. This approach has no free parameters. It overcomes some theoretical shortcomings of the original form of the Dirac impulse approximation,[6,7] denoted IA1, which predicts the Dirac optical potential from knowledge of positive-energy *NN* scattering data.[8]

The original (IA1) form of the Dirac impulse approximation successfully predicts the spin observables in proton-nucleus elastic scattering above about 300 MeV.[9,10] However, the specification of the optical potential is incomplete due to reliance on five Fermi covariants and associated amplitudes to extrapolate the *NN* scattering operator from the positive energy sector, where it is determined by *NN* scattering experiments, to the full Dirac space of two nucleons. Fermi covariants involve a pseudoscalar term in the parametrization of on-shell invariants.[2] This results in overly strong scalar and vector components of the Dirac optical potential at low energies. Moreover, the predictions for nucleon-nucleus scattering depend on the prediction of couplings involving negative-energy basis states of the free Dirac equation.[11,12] These control the virtual-pair couplings but they cannot be obtained unambiguously from the matrix elements involving only positive-energy states.

The ambiguity of the IA1 approach is overcome in the generalized impulse approximation, IA2, by adopting a relativistic meson-exchange description of the nuclear force[13-15] as the dynamical basis for extending the *NN* data to all sectors of the Dirac space of two nucleons. Pseudovector πN coupling and vertex cutoffs are incorporated to maintain sensible behavior at low energy and at large momentum. The resulting meson-exchange model succeeds in explaining *NN* scattering observables from 0 to 1000 MeV and it provides a prediction for the negative-energy couplings needed to construct the optical potential. No other way of comparable sophistication exists to predict the required negative-energy couplings. The meson-exchange model is based on an effective Lagrangian similar to ones conventionally used to calculate meson-exchange currents in electromagnetic reactions. Thus the IA2 approach unifies the theoretical description of nucleon-nucleus scattering with that of NN scattering and to a certain extent with that of meson-exchange currents.

The *NN* interaction analysis involves coupled *NN*, $N\Delta$, and $\Delta\Delta$ integral equations with meson-exchange kernels. These equations are solved using a quasipotential reduction of the coupled Bethe-Salpeter dynamics developed by van Faassen and Tjon.[14] A straightforward extension is made to include negative-energy intermediate states,[4] and calculations are performed to determine a complete set of *NN* helicity amplitudes for each proton energy of interest. This analysis is performed in the center-of-mass frame of two nucleons since that is the only practical frame for partial wave analysis. However, the optical potential is needed in the nucleon-nucleus c.m. frame. It is convenient to convert to a Lorentz-invariant description, consisting of a sum of Lorentz-invariant amplitudes times kinematical covariants, in order to obviate the boost problem. The *NN* helicity amplitudes in the c.m. frame are used to determine the Lorentz-invariant amplitudes of the *NN* scattering operator.

Freedom exists in the choice of kinematical covariants of the Lorentz-invariant representation. There are many ways to choose a complete and linearly independent set. The situation is analogous to that for the choice of basis functions with which to expand an arbitrary state vector in quantum mechanics. Any basis set will do in principle if it is complete. Symmetry and simplicity dictate the choice for a given problem that is most appropriate. The choice of kinematical covariants given in Ref. 5 incorporates Pauli exchange antisymmetry in a very simple fashion. This is particularly useful for the separation of direct and exchange contributions to the *NN* amplitude. Kinematical covariants are symmetric or antisymmetric with respect to exchange of the two nucleons. Consequently the associated Lorentz-invariant amplitudes are symmetric or antisymmetric with respect to interchange of the Mandelstam arguments, t and u. This interchange is equivalent to $\theta \rightarrow \pi - \theta$, where θ is the c.m. scattering angle. Thus the exchange symmetry required by the Pauli principle is manifest in each amplitude rather than being spread over many amplitudes as is the case for other choices of kinematical covariants in the literature. Analytical fits to the *NN* amplitudes are given in Ref. 5 in terms of Yukawa functions of t (direct terms) and Yukawa functions of u (exchange terms).

Using the complete sets of Lorentz-invariant amplitudes, the Dirac optical potential is constructed as shown in detail in Ref. 3. In this paper, systematic calculations are presented based on that formalism. Comparisons are made with the original form of the Dirac impulse approximation and with the traditional Schrödinger impluse approximation. In Sec. II, the theoretical calculations are outlined and some conventions used in the paper are given. Section III presents potentials used in the Dirac equation and also presents potentials for the Schrödinger equation which produce equivalent scattering amplitudes. The latter are separated into "no-pair" parts and virtual-pair contributions. Results for elastic proton scattering are compared with experimental data in Sec. IV. Various refinements of the original impulse approximation have been prescribed to incorporate pseudovector πN coupling. In Sec. V these are compared with the IA2 analysis which consistently embeds pseudovector coupling. The role of numerically small tensor, scalar spin-orbit, and vector spin-orbit potentials in the Dirac analysis is considered in Sec. VI. A summary and outlook are presented in Sec. VII.

II. DESCRIPTION OF THE CALCULATIONS

The analysis of the Dirac optical potential is carried out most naturally in momentum space. However, for computational simplicity, a localized potential is used in this paper to permit coordinate-space analysis. The potential is developed from the momentum-space expression

$$\hat{U}(\mathbf{p},\mathbf{q}) = -\tfrac{1}{4}\mathrm{Tr}_2[\hat{M}(p,-\tfrac{1}{2}q \rightarrow p-q,+\tfrac{1}{2}q)\hat{\rho}(\mathbf{q})] , \tag{1}$$

where $\hat{M}(p,-\tfrac{1}{2}q \rightarrow p-q,+\tfrac{1}{2}q)$ is the Breit frame *NN* scattering operator in the Dirac space of two nucleons and $\hat{\rho}(\mathbf{q})$ is the relativistic nuclear density. Conventionally, particle 2 is the target nucleon, and the trace is over the Dirac indices of particle 2. This form of potential is appropriate for closed-shell nuclei, for which the relativistic nuclear density consists of scalar, vector, and tensor components as follows:

$$\hat{\rho}(\mathbf{q}) = \rho_S(q) + \gamma_2^0 \rho_V(q) - \frac{\alpha_2 \cdot \mathbf{q}}{2m}\rho_T(q) . \tag{2}$$

Nuclear form factors, $\rho_S(q)$, $\rho_V(q)$, and $\rho_T(q)$, are determined from the relativistic Hartree wave functions of Horowitz and Serot.[16] Neutron-proton differences are incorporated by evaluating Eq. (1) twice, once with the proton-proton amplitude, $\hat{M}_{pp}$, together with the proton density, $\hat{\rho}_p$, and once with the proton-neutron amplitude, $\hat{M}_{pn}$, together with the neutron density, $\hat{\rho}_n$. The two results are added to determine the optical potential.

After localization to permit coordinate-space analysis, the problem comes down to solving the Dirac equation,

$$[E\gamma^0 + i\gamma\nabla - m - \hat{U}(\mathbf{r})]\psi(\mathbf{r}) = 0 , \tag{3}$$

where $E = (k^2 + m^2)^{1/2}$ and k is the on-shell momentum in the proton-nucleus c.m. frame. In general, the potential can contain eight terms. However, only six nonvanishing terms are found in the analysis of Ref. 3. Two terms, involving Dirac operators which are odd with respect to time reversal, are found to be zero. Moreover, a transformation eliminates a space-vector term. Thus the potential, in its final form, contains five terms due to the strong interaction. In addition, there are two electromagnetic terms as follows:

$$\begin{aligned}\hat{U}_{\mathrm{IA2}}(\mathbf{r}) = {} & \tilde{S}(r) + \gamma^0[\tilde{V}(r) + V_C(r)] - i\alpha\cdot\hat{r}[\tilde{T}(r) + T_C(r)] \\ & -[\tilde{S}_{LS}(r) + \gamma^0\tilde{V}_{LS}(r)]\sigma\cdot\mathbf{L} .\end{aligned} \tag{4}$$

The strong interaction potentials $\tilde{S}$, $\tilde{V}$, $\tilde{T}$, $\tilde{S}_{LS}$, and $\tilde{V}_{LS}$ are defined in Eqs. (4.16)–(4.21) of Ref. 3. The electromagnetic potentials, V_C and T_C, are determined by

$$\begin{aligned}&\int d^3r\, e^{i\mathbf{q}\cdot\mathbf{r}}[V_C(r) - i\alpha\cdot\hat{r}T_C(r)] \\ &\qquad = \frac{Z\alpha}{\mathbf{q}^2}\left[\gamma^0 F_1(q^2) - i\frac{\kappa}{2m}\alpha\cdot\mathbf{q}F_2(q^2)\right]\rho_{\mathrm{ch}}(\mathbf{q}) ,\end{aligned} \tag{5}$$

where F_1 and F_2 are proton form factors, κ is the proton anomalous magnetic moment, and ρ_{ch} is the charge form factor of the nucleus.

Calculations are also presented for the IA1 impulse approximation. In that case one has three terms due to the strong interaction plus two electromagnetic terms as follows:

$$\hat{U}_{\mathrm{IA1}}(\mathbf{r})=S(r)+\gamma^0[V(r)+V_C(r)] -i\alpha\cdot\hat{r}[T(r)+T_C(r)]\ . \tag{6}$$

The difference is that a complete set of *NN* amplitudes is used in Eq. (1) to determine $\hat{U}_{\mathrm{IA2}}$, while the five Fermi amplitudes are used to determine $\hat{U}_{\mathrm{IA1}}$. This difference only affects the negative-energy couplings in the plane-wave basis of Dirac states, i.e., the same *NN* amplitudes are used in positive-energy states for IA1 and IA2. Moreover, phenomenological phase shifts[17] are used to construct the positive-energy amplitudes.

Comparisons of the relativistic impulse approximation are made to the corresponding nonrelativistic impulse approximation which is denoted NRIA. NRIA calculations are usually based on solving the Schrödinger equation with relativistic kinematics using an optical potential based on Pauli *NN* amplitudes, *A* and *C*, determined from positive-energy matrix elements of the full *NN* scattering operator, $\hat{M}$, as follows:

$$\bar{u}_1^{(+)}(\mathbf{p}_1')\bar{u}_2^{(+)}(\mathbf{p}_2')\hat{M}u_1^{(+)}(\mathbf{p}_1)u_2^{(+)}(\mathbf{p}_2) =\chi_1'^{\dagger}\chi_2'^{\dagger}\left[A+iC\sigma_1\cdot\mathbf{q}\frac{\mathbf{p}_1'+\mathbf{p}_1}{2}+\cdots\right]\chi_1\chi_2\ , \tag{7}$$

where the omitted terms on the right side involve the spin operator σ_2. (See Ref. 8 for details of the connection of Pauli amplitudes to invariant amplitudes.) Only the *A* and *C* Pauli terms contribute to the optical potential for a closed-shell nucleus. Central and spin orbit potentials are determined by

$$N_C(r)=(2\pi)^{-3}\int d^3q\, e^{-i\mathbf{q}\cdot\mathbf{r}}A(q)\rho_{\mathrm{nr}}(q)\ , \tag{8}$$

$$i\mathbf{r}N_{LS}(r)=(2\pi)^{-3}\int d^3q\, e^{-i\mathbf{q}\cdot\mathbf{r}}\mathbf{q}C(q)\rho_{\mathrm{nr}}(q)\ , \tag{9}$$

where $\rho_{\mathrm{nr}}(q)$ is the Fourier transform of the nonrelativistic matter density. These potentials are used in the Schrödinger equation with relativistic kinematics, e.g.,

$$\left[\frac{k^2-p^2}{E+m}-N_C(r)-N_{LS}(r)\sigma\cdot L\right]\psi=0\ . \tag{10}$$

Here $E+m$ replaces $(A-1)/A$ times twice the reduced mass of the Kerman, McManus, and Thaler (KMT) approach,[18] where *A* is the number of nucleons in the target nucleus. Other prescriptions for incorporating relativistic kinematics are sometimes used, but they are essentially equivalent to this one. Equation (10) is preferred because it has a natural correspondence with a "no-pair" approach. As written, Eq. (10) omits electromagnetic effects. When these are incorporated, Eq. (10) is equivalent to solving the Dirac equation (3) with the potential

$$\hat{U}_{\mathrm{NRIA}}(r)=\left[\frac{1+\gamma^0}{2}\right][N_C(r)+N_{LS}(r)\sigma\cdot\mathbf{L}] +\gamma^0V_c(r)-i\alpha\cdot\hat{\mathbf{r}}T_C(r)\ . \tag{11}$$

This follows because terms involving $(1+\gamma^0)$ act only in the equation for the upper component of the Dirac wave function. When the Dirac equation with the potential of Eq. (11) is reduced to an equivalent Schrödinger equation, omitting Coulomb effects, Eq. (10) is obtained. Comparison of Eq. (11) with Eq. (4) shows that the NRIA analysis may be performed by solving the Dirac equation using the potential based on $\tilde{S}=\tilde{V}=\frac{1}{2}N_C(r)$, $\tilde{S}_{LS}=\tilde{V}_{LS}=-\frac{1}{2}N_{LS}$, and $\tilde{T}=0$ in Eq. (4).

Equivalent Schrödinger central and spin-orbit potentials are defined such that the scattering is the same based on the Dirac and Schrödinger equations. This is accomplished by writing the Dirac equation as coupled equations for the upper- and lower-component wave functions, solving for the lower-component wave function, and substituting the result into the equation for the upper-component wave function. After some manipulation one obtains a standard form Schrödinger equation. The Appendix shows how the Dirac equation with five terms in the potential as in (4) is manipulated to the Schrödinger equation (10) with equivalent central and spin-orbit potentials, U_C and U_{LS}, in place of the nonrelativistic potentials.

Differences between the equivalent Schrödinger potentials, U_C and U_{LS}, derived from the full set of Dirac potentials and the NRIA Schrödinger potentials, N_C and N_{LS}, of Eqs. (8) and (9), are due to inclusion of virtual-pair effects in the Dirac analysis. The NRIA approach corresponds to eliminating all virtual-pair effects by not permitting any negative-energy couplings of the Dirac potential with respect to the plane-wave basis of Dirac states.

In this paper, the Schrödinger theory with relativistic kinematics is defined as the "no-pair" theory obtained from a relativistic theory by eliminating all negative-energy couplings with respect to the plane-wave basis of Dirac states. This definition clarifies exactly what we mean by Schrödinger theory with relativistic kinematics. By this definition, the NRIA optical potential is equivalent to the "no-pair" Dirac potential which one obtains by evaluating Eq. (1) using a positive-energy projected *NN* scattering operator, i.e.,

$$\hat{M}_{\text{no pair}}=\Lambda_1^{(+)}(p_1')\Lambda_2^{(+)}(\mathbf{p}_2')\hat{M}\Lambda_1^{(+)}(\mathbf{p}_1)\Lambda_2^{(+)}(\mathbf{p}_2)\ , \tag{12}$$

where

$$\Lambda_i^{(+)}(\mathbf{p})=(E_p\gamma_i^0-\gamma_i\cdot\mathbf{p}+m)/(2m)\ ,$$

and using $\rho_V=\rho_S=\rho_T=\rho_{\mathrm{nr}}$ in Eq. (2). In the "no-pair" analysis, one obtains a Dirac potential as in Eq. (4) and this can then be converted to an equivalent Schrödinger potential as shown in the Appendix. The resulting "no-pair" Schrödinger potentials are only slightly different from the usual nonrelativistic potentials of Eqs. (8) and (9). We find that the "no-pair" potential, determined using Eqs. (12) in Eq. (2), produces equivalent results for proton scattering to those obtained using the usual NRIA potential of Eqs. (8) and (9). Inconsequential differences arise because momentum dependence in Dirac spinors, e.g., $U_2^{(+)}(\mathbf{p}_2)$ in Eq. (7), are treated a little differently in the optical potential formalism of Ref. 3.

III. DIRAC AND EQUIVALENT SCHRÖDINGER POTENTIALS

Consider the Dirac equation with a five-term optical potential as in Eq. (4). As noted above, this is obtained from an equation with a six-term optical potential by use of a wave function transformation which absorbs a space-vector term, $C(r)$. In Figs. 1–4, the strong interaction potentials based on the generalized impulse approximation, IA2, are shown for proton scattering from ^{40}Ca at energies 200, 500, and 800 MeV. Note that as the energy increases the scalar and vector potentials decrease slowly, i.e., there is rather little energy dependence. This is also true for spin-orbit terms, $\tilde{S}_{LS}(r)$ and $\tilde{V}_{LS}(r)$, which are much smaller in magnitude. The tensor term has a real part that increases in magnitude with increasing energy; however, the imaginary part decreases. The space-vector term, $C(r)$, not shown in Eq. (4) due to being absorbed by a transformation of the wave function, enters the Dirac equation as

$$[C(r)/m](E\gamma^0+i\gamma\nabla-m) .$$

The relevant scale for this potential is the nucleon mass, m. $C(r)$ differs from the other potentials in that its imaginary part increases in magnitude as the energy increases, while its real part varies from positive to negative. The factor $C(r)/m$ has a magnitude of about 0.05.

IA1 provides very good descriptions of proton elastic scattering at 500 and 800 MeV from ^{40}Ca based on scalar, vector, and tensor potentials only. However, the scalar and vector potentials are too large at lower proton energies.[2] One objective of IA2 is to remedy this situation. As seen in Fig. 5, IA2 succeeds in this objective. At the center of the nucleus, the real part of S changes from approximately -490 MeV for IA1 to -250 MeV for IA2. The real part of the vector potential changes from approximately 410 MeV for IA1 to 190 MeV for IA2. The imaginary parts of both scalar and vector potentials are reduced greatly.

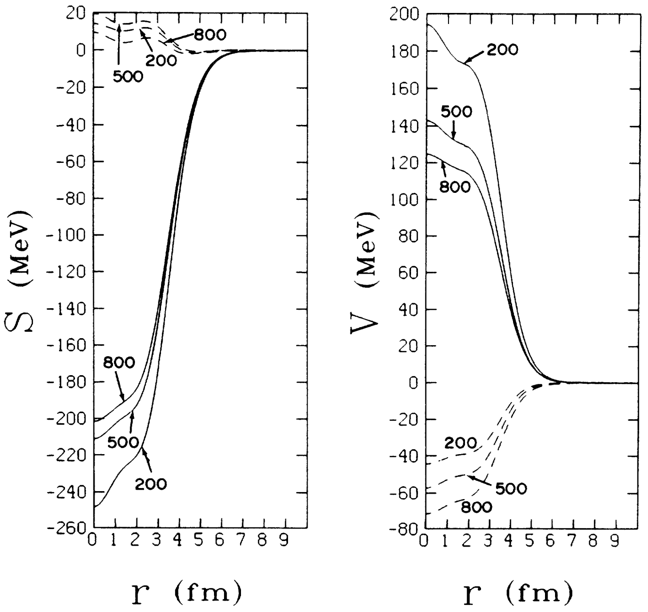

FIG. 1. The left panel shows the scalar potential for ^{40}Ca at 200, 500, and 800 MeV using the IA2. The right panel shows the vector potential. The solid line is the real part and the dashed line is the imaginary part.

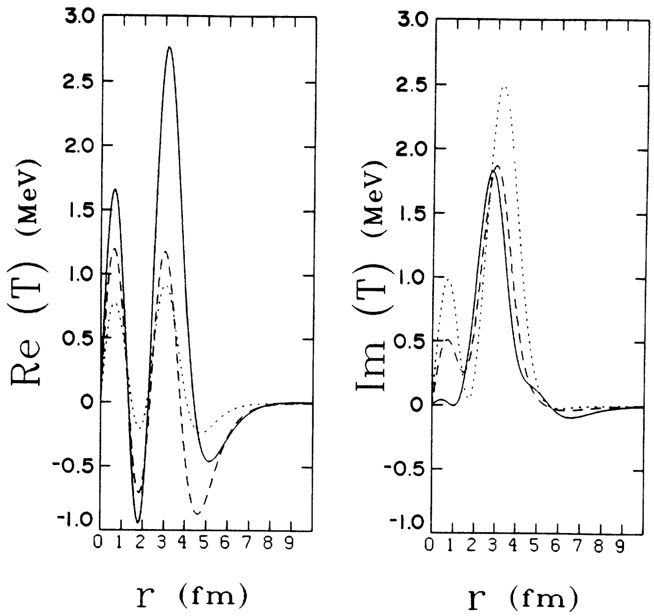

FIG. 2. The tensor potential for ^{40}Ca at 200, 500, and 800 MeV using the IA2. The left panel shows the real part. The right panel shows the imaginary part. The solid line is 800 MeV, the dashed line is 500 MeV, and the dotted line is 200 MeV.

The Appendix outlines the derivation of equivalent Schrödinger central and spin-orbit potentials, U_C and U_{LS}, from the five-term Dirac potential. These Schrödinger potentials are separated into two parts as follows:

$$U_C=N_C+P_C , \tag{13}$$

$$U_{LS}=N_{LS}+P_{LS} , \tag{14}$$

where N_C and N_{LS} are equivalent Schrödinger "no-pair" potentials determined as described following Eq. (12). They are essentially the same as the NRIA potentials of Eqs. (8) and (9). P_C and P_{LS} are virtual $N\bar{N}$ pair potentials defined by these equations. Thus the NRIA analysis involves solving the Schrödinger equation with the "no-pair" potentials only. The new ingredients obtained by solving the Dirac equation with the IA2, IA1, or other relativistic approaches, are the central and spin-orbit terms, P_C and P_{LS}, of the equivalent Schrödinger equation.

Figure 6 shows the pair potentials and Fig. 7 shows the "no-pair," or nonrelativistic, potentials for ^{40}Ca at energies 200, 500, and 800 MeV. In general these potentials are functions of r and orbital angular momentum, ℓ. The ℓ dependence is rather smooth, and Figs. 6 and 7 show results for $\ell=0$. One observes that the pair potentials are quite large and they vary little throughout this energy range. The situation is qualitatively different from that for medium modifications, such as Pauli blocking, which fade away with increasing energy. The bulk of the energy dependence in the Schrödinger equivalent potentials is in the "no-pair" terms as shown in Fig. 7.

Pair potentials for IA2 are substantially smaller than for IA1 at 200 MeV and at lower energies. Figure 8 shows the pair potentials at 200 MeV. The "no-pair" potentials based on IA2 and IA1 are the same. Differences in the pair potentials are due mainly to the use of pseudovector πN coupling in the IA2 analysis versus the

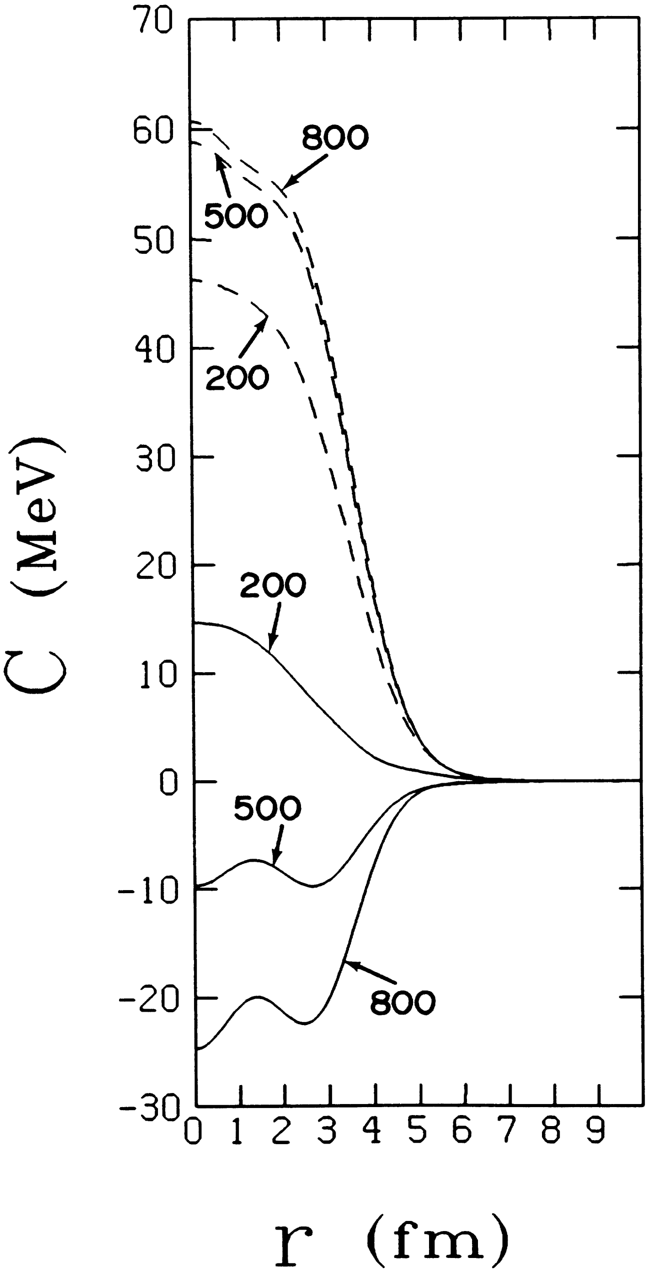

FIG. 3. The space-vector potential for ^{40}Ca at 200, 500, and 800 MeV using the IA2. The solid line is the real part and the dashed line is the imaginary part.

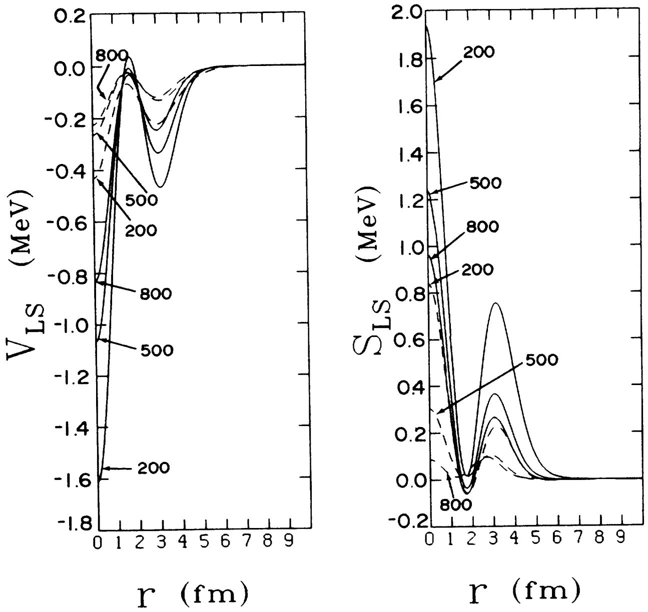

FIG. 4. The left panel shows the vector spin-orbit potential for ^{40}Ca at 200, 500, and 800 MeV using the IA2. The right panel shows the scalar spin-orbit potential. The solid line is the real part and the dashed line is the imaginary part.

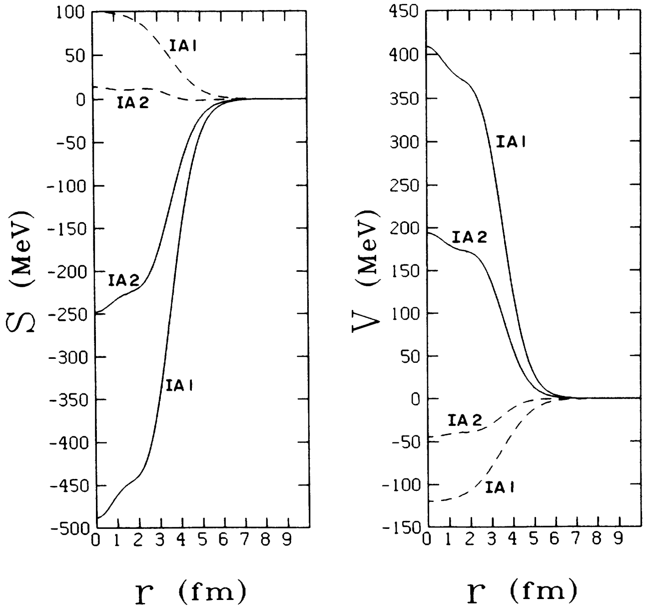

FIG. 5. The left panel shows the scalar potential for ^{40}Ca at 200 MeV based on the IA2 and based on the IA1. The right panel shows the vector potential for ^{40}Ca at 200 MeV based on the IA2 and based on the IA1. The solid line is the real part and the dashed line is the imaginary part.

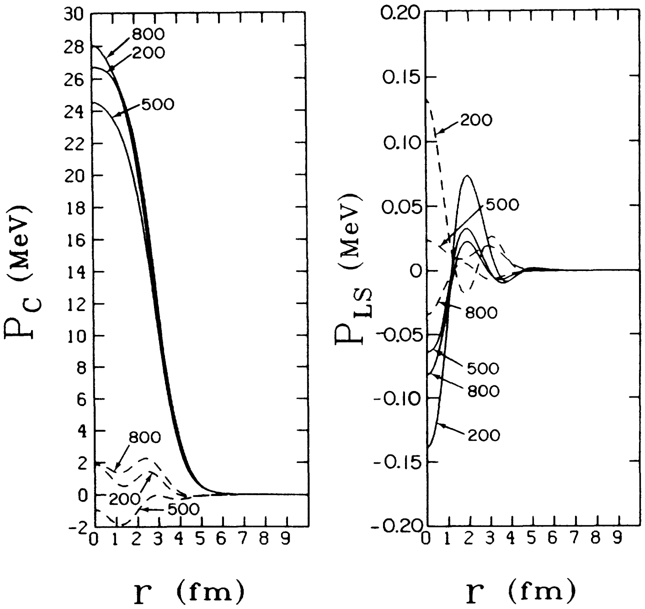

FIG. 6. The ^{40}Ca equivalent Schrödinger pair potentials for 800, 500, and 200 MeV. The left panel shows the central potential; the right panel shows the spin-orbit potential. The solid line is the real part and the dashed line is the imaginary part.

pseudoscalar parametrization of the on-shell invariants in the IA1 analysis. Real pair potentials at 200, 500, and 800 MeV are reduced in IA2 by about 60%, 50%, and 40%, respectively, when compared with IA1 results. There is rather little energy dependence of the pair potential in IA2.

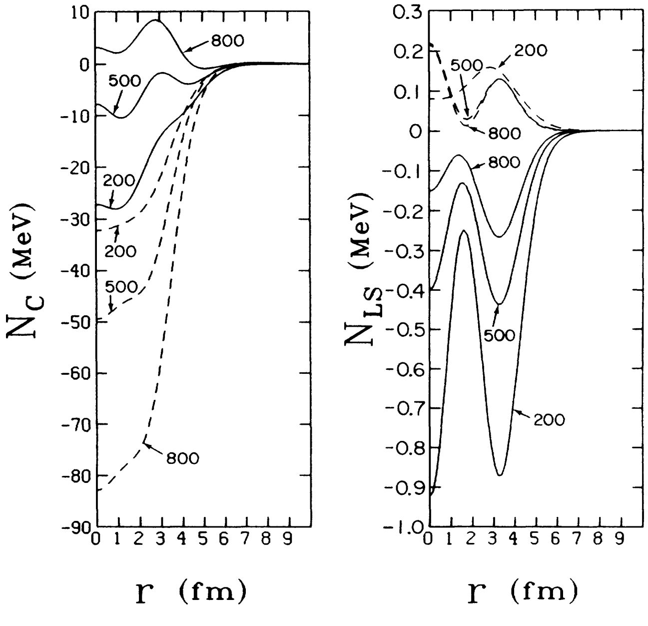

FIG. 7. The ^{40}Ca equivalent Schrödinger "no-pair" potentials for 800, 500, and 200 MeV. The left panel shows the central potential; the right panel shows the spin-orbit potential. The solid line is the real part and the dashed line is the imaginary part.

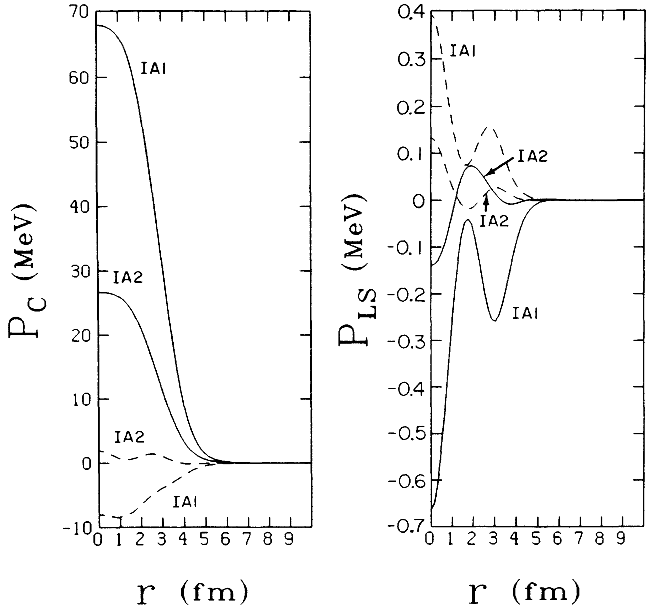

FIG. 8. The pair potentials for 200 MeV proton scattering from ^{40}Ca based on the IA2 and the IA1. The solid lines show the real parts and the dashed lines show the imaginary parts.

A recent analysis of Pauli-blocking effects[19] in the Dirac approach is based on multiplying the scalar and vector potentials by Pauli reduction factors. The Pauli factors are calculated in nuclear matter and they are extrapolated to finite nuclei using a local-density approximation. We have applied the scalar and vector reduction factors of Ref. 19 to the corresponding potentials of the IA2 approach to arrive at an estimate of the Pauli-blocking effect. Transforming the Pauli-blocked scalar and vector potentials to the equivalent Schrödinger equation, we find that there is medium modification of the central pair potential, P_C, but scarcely any effect on N_C, N_{LS}, or P_{LS} outside of a slight reduction of the imaginary part of the no-pair potential N_C near $r=0$. This is surprising because in nonrelativistic treatments, the entire effect of Pauli blocking occurs in the "no-pair" potentials. A future article will consider Pauli blocking based upon the *NN* integral equations of the IA2 approach. In this work, the very simple blocking factors of Ref. 19 are employed to make an estimate of the Pauli-blocking effects and to compare them with the correction due to pair terms of the IA2 analysis.

Figure 9 compares the equivalent Schrödinger potentials at 200 MeV for three cases: (1) potentials U and U based on IA2 without Pauli-blocking corrections; (2) potentials U_C and U_{LS} based on IA2 with Pauli-blocking corrections; and (3) potentials N_C and N_{LS}, the "no-pair" or nonrelativistic potentials. Pauli blocking is seen to decrease the central potential, U_C, significantly but to have little effect on the spin-orbit potential. Inclusion of pair terms produces a larger modification of the central potential, one which does not fade away with increasing energy in the 200–800 MeV range. This behavior is expected to be general in nature.

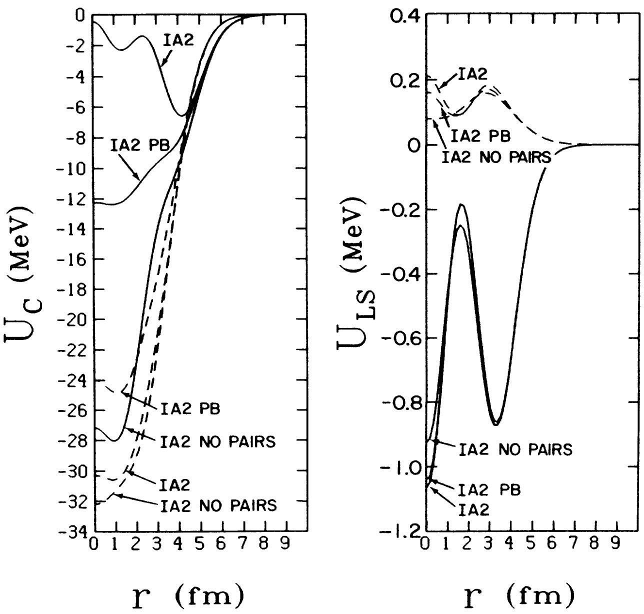

FIG. 9. The full equivalent Schrödinger potentials at 200 MeV. The IA2 curves are based on the impulse approximation, the IA2PB curves include Pauli blocking, and "no-pair" curves omit virtual pair contributions. The left panel shows central potentials and the right panel shows the spin-orbit potentials.

IV. ENERGY AND TARGET SURVEY

In our calculations, two sets of densities are used to describe the target nuclei. For ^{208}Pb and ^{40}Ca, all the results shown in this paper are based on the relativistic Hartree densities of Ref. 16. Similar results are obtained using the densities of Ref. 20 which are matter vector densities for protons fitted to the experimental charge densities and matter vector densities for neutrons fitted to the Gogny and DeCharge Hartree-Fock-Bogoliubov neutron densities.[21] Comparisons of the two densities are based on using the predictions of the relativistic Hartree model to constrain the differences between scalar and vector densities and similarly the differences between tensor and vector densities. We find that proton scattering results are essentially the same for either density set for calcium and lead. However, a significant improvement of the cross section is obtained by using the densities of Ref. 20 for oxygen. For this reason all our results for ^{16}O are based on the densities of Ref. 20. In general, only the cross sections display much sensitivity to the differences between the two densities.

Figures 10–18 show the proton scattering observables for ^{40}Ca, ^{208}Pb, and ^{16}O at 200, 500, and 800 MeV. Each figure shows the IA2 result (solid line), the IA1 result (dashed line), and the NRIA result (dotted line).

A. ^{40}Ca

For the cross section, analyzing power (A_Y), and spin rotation parameter (Q), there is a significant improvement with IA2 at 200 MeV. As is shown in Fig. 10, the cross section has more oscillatory structure than the data[22,23] in all three cases. There is less difference between IA2 and IA1 results than between either of these and the NRIA results. Substantial differences are obtained for A_Y and Q. IA2 yields an excellent reproduction of the spin data, and this is a significant improve-

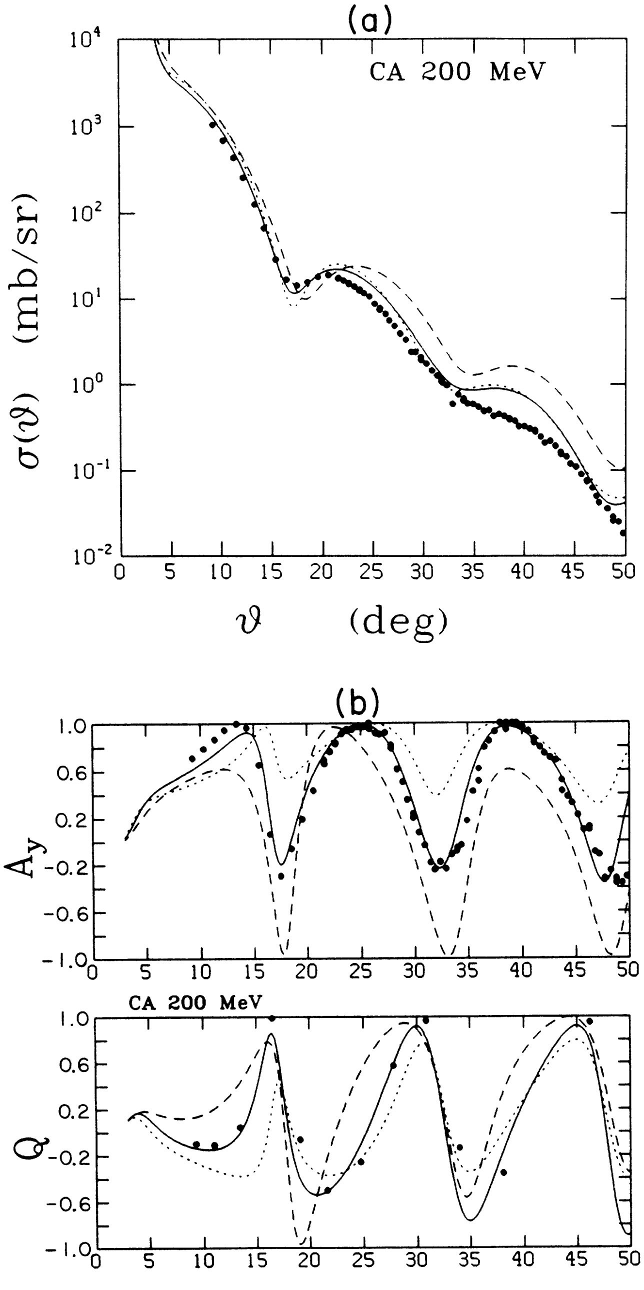

FIG. 10. The differential cross section, analyzing power (A_Y), and spin rotation function (Q) for 200 MeV protons scattering from ^{40}Ca. The solid line shows the IA2 result, the dashed line shows the IA1 result, and the dotted line shows the NRIA result. The data are from Refs. 22 and 23.

ment over IA1 and NRIA. The sizable differences between the three calculations are attributable to virtual-pair contributions as noted already.

Both IA1 and IA2 results provide a good description of the data[24,25] at 500 MeV as seen in Fig. 11. For the cross section, the IA2 result is closest to the experimental data; however, the IA1 result excels in reproducing the first diffraction minimum. At larger angles, the IA2 result excels. The failure of the NRIA first was pointed out[24] in the analysis of these data at 500 MeV, particularly with regard to the failure to predict the analyzing power. For A_Y, the IA1 result excels, especially over the

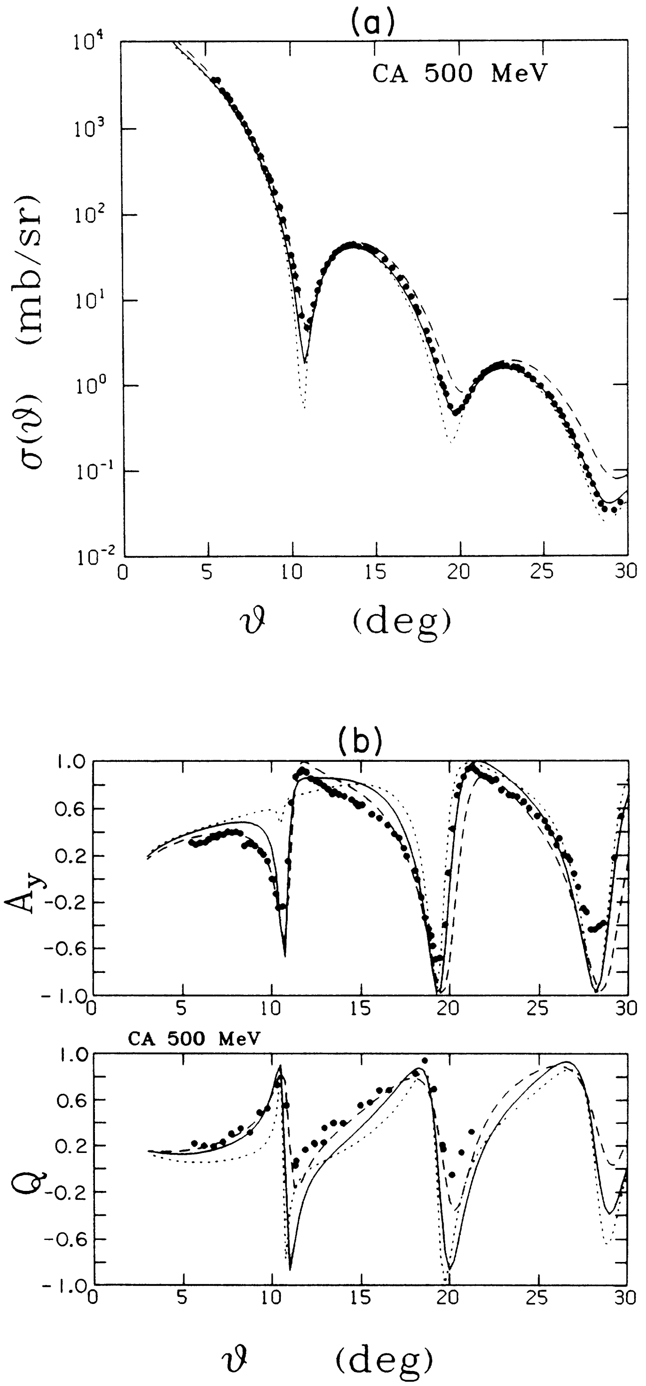

FIG. 11. The differential cross section, analyzing power (A_Y), and spin rotation function (Q) for 500 MeV protons scattering from ^{40}Ca. The solid line shows the IA2 result, the dashed line shows the IA1 result, and the dotted line shows the NRIA result. The data are from Refs. 24 and 25.

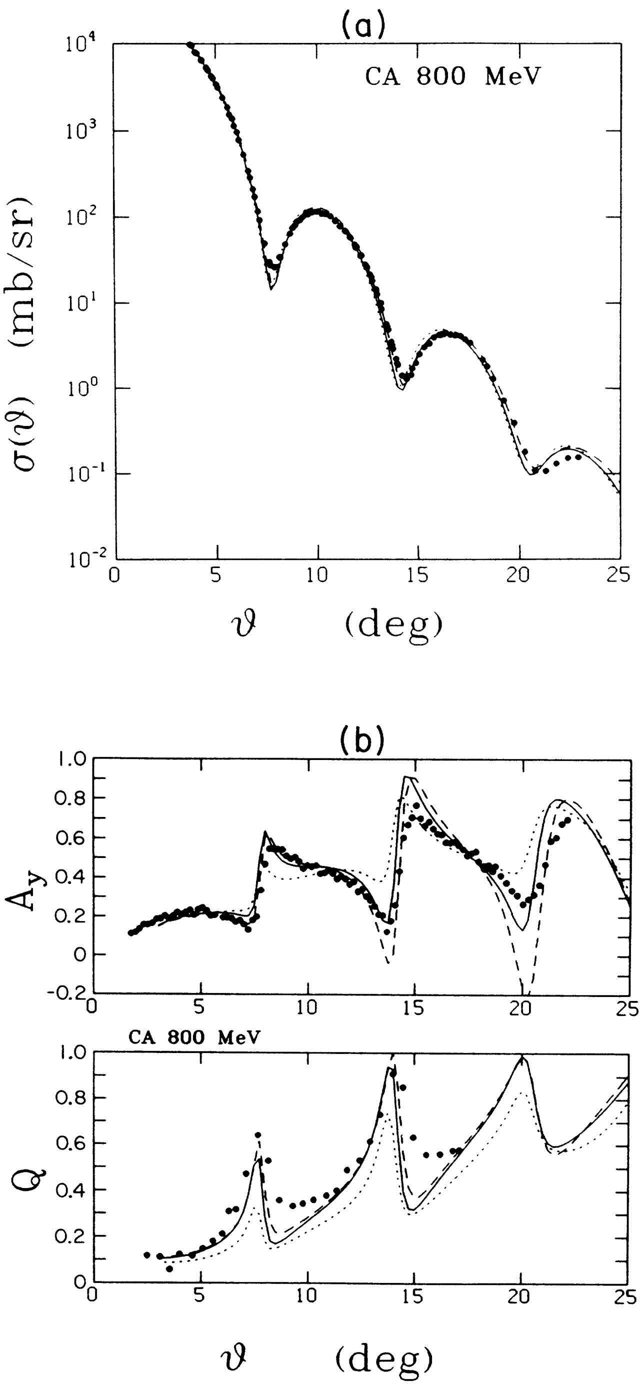

FIG. 12. The differential cross section, analyzing power (A_Y), and spin rotation function (Q) for 800 MeV protons scattering from ^{40}Ca. The solid line shows the IA2 result, the dashed line shows the IA1 result, and the dotted line shows the NRIA result. The data are from Refs. 10 and 20.

first 17 deg or so. For larger angles, there is not much difference between the three curves. For small scattering angles, the IA2 result is much better than the NRIA result. For the Q observable, the IA1 result provides the closest reproduction of the experimental data. The IA2 result is a significant improvement over the NRIA result through about 10 deg, but it does not describe the data as well as the IA1 result. This is apparently due to the smaller scalar and vector potentials in the IA2 approach.

At 800 MeV, IA1, IA2, and NRIA results shown in

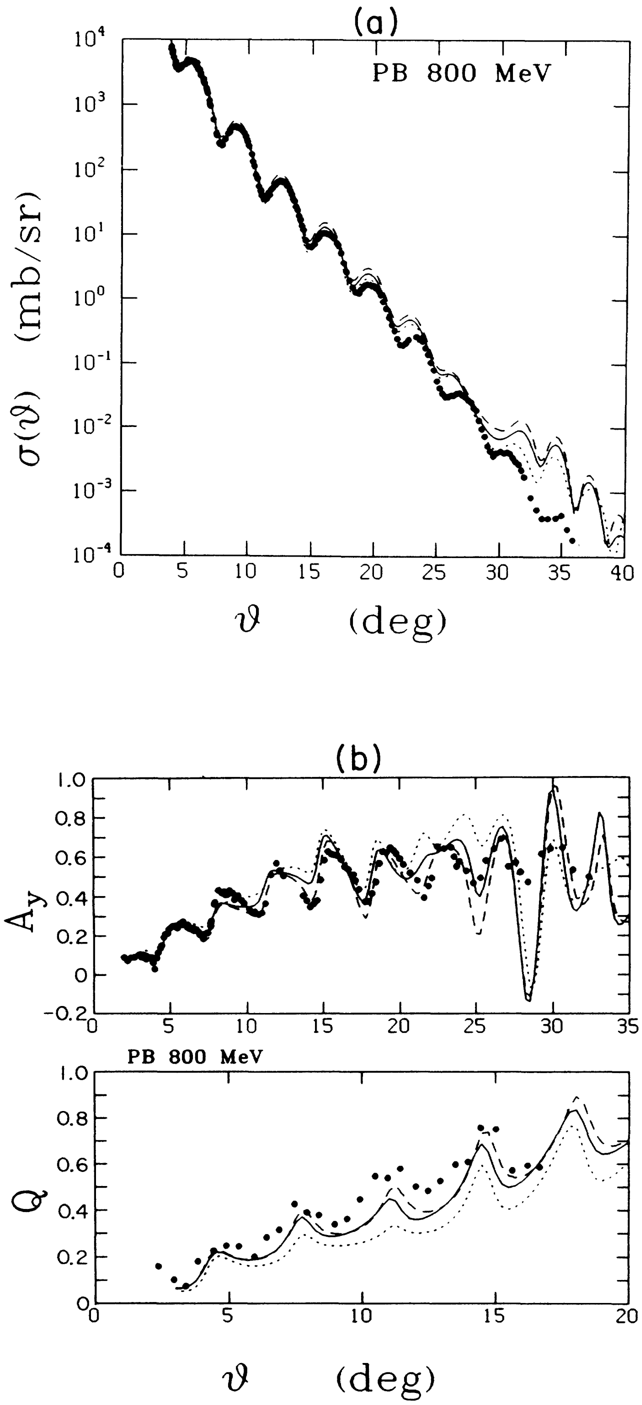

FIG. 13. The differential cross section, analyzing power (A_Y), and spin rotation function (Q) for 800 MeV protons scattering from ^{208}Pb. The solid line shows the IA2 result, the dashed line shows the IA1 result, and the dotted line shows the NRIA result. The data are from Ref. 26.

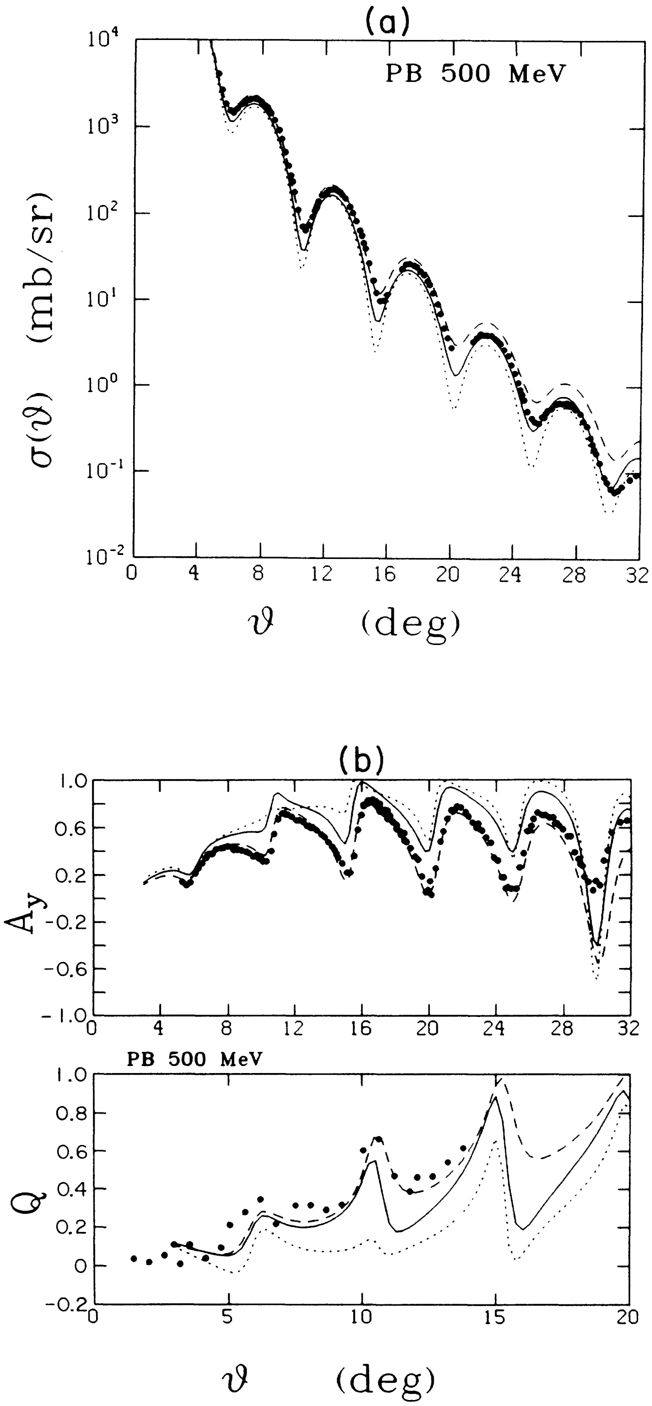

FIG. 14. The differential cross section, analyzing power (A_Y), and spin rotation function (Q) for 500 MeV protons scattering from ^{208}Pb. The solid line shows the IA2 result, the dashed line shows the IA1 result, and the dotted line shows the NRIA result. The data are from Refs. 10 and 20.

Fig. 12 are all quite similar. Each provides a good description of the cross section[10] up to about 20 deg, and each fails at larger angles. For spin observables A_Y and Q,[20] the IA2 and IA1 results are very close to each other and somewhat superior to the NRIA result.

B. ^{208}Pb

As for ^{40}Ca at 800 MeV, there is not much difference between IA2, IA1, and NRIA results for ^{208}Pb at 800 MeV, as shown in Fig. 13. Each describes the cross sec-

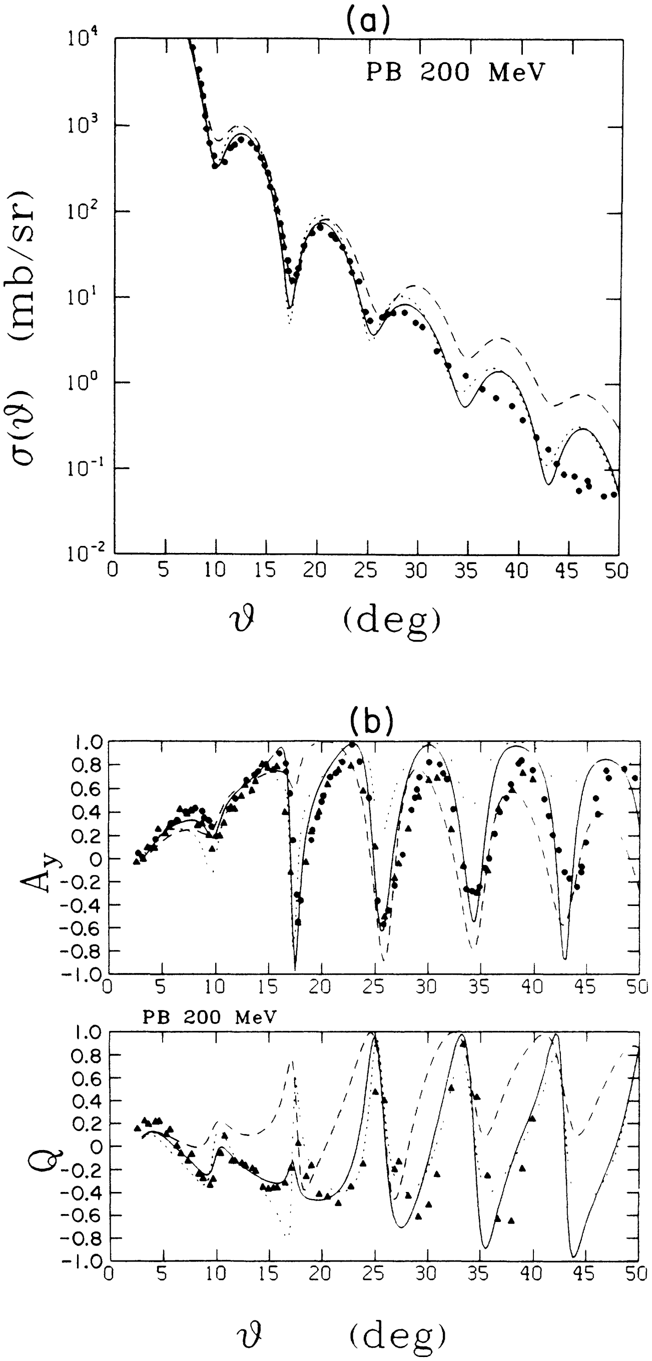

FIG. 15. The differential cross section, analyzing power (A_Y), and spin rotation function (Q) for 200 MeV protons scattering from ^{208}Pb. The solid line shows the IA2 result, the dashed line shows the IA1 result, and the dotted line shows the NRIA result. The data are from Refs. 28 (circles) and 29 (triangles).

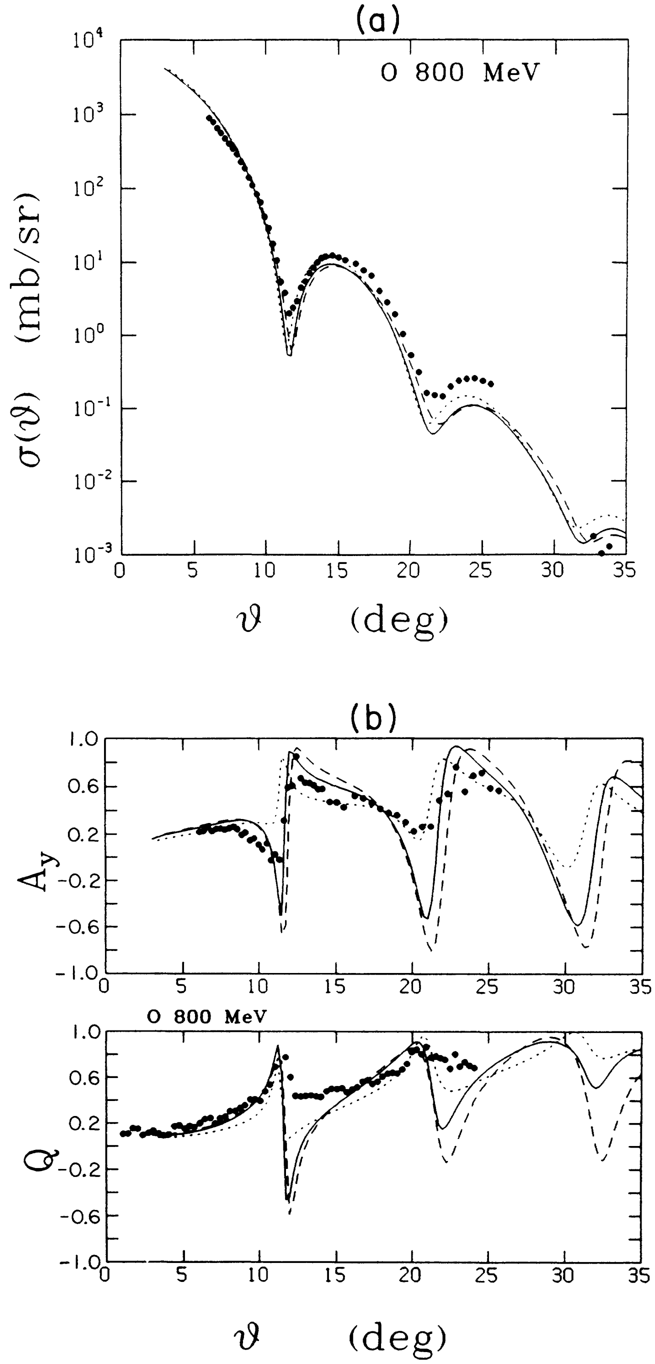

FIG. 16. The differential cross section, analyzing power (A_Y), and spin rotation function (Q) for 800 MeV protons scattering from ^{16}O. The solid line shows the IA2 result, the dashed line shows the IA1 result, and the dotted line shows the NRIA result. The data are from Ref. 30.

tion[26] through about 20 deg, but each worsens at larger angles. They are also quite close with regard to describing the A_Y and Q data. Overall, there seem to be no large differences.

Sharper differences occur at 500 MeV, as shown in Fig. 14. The NRIA result is clearly worse than either the IA2 or IA1 result. For the cross section the IA2 prediction is best after about 20 deg, but the IA1 prediction is closer to experiment[10,20] at smaller angles. Again this is due to the smaller scalar and vector potentials. The comparison with A_Y data in Fig. 14 provides the most notable discrepancy between the IA2 calculation and spin observ-

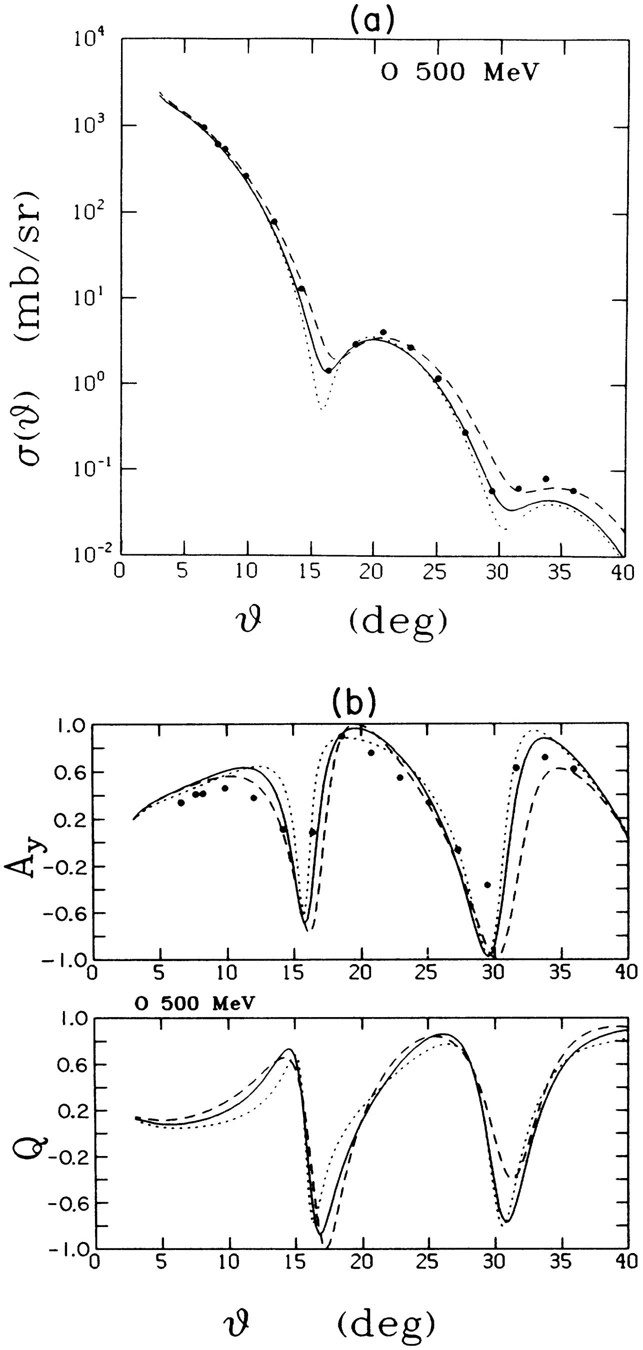

FIG. 17. The differential cross section, analyzing power (A_Y), and spin rotation function (Q) for 500 MeV protons scattering from ^{16}O. The solid line shows the IA2 result, the dashed line shows the IA1 result, and the dotted line shows the NRIA result. The data are from Ref. 31.

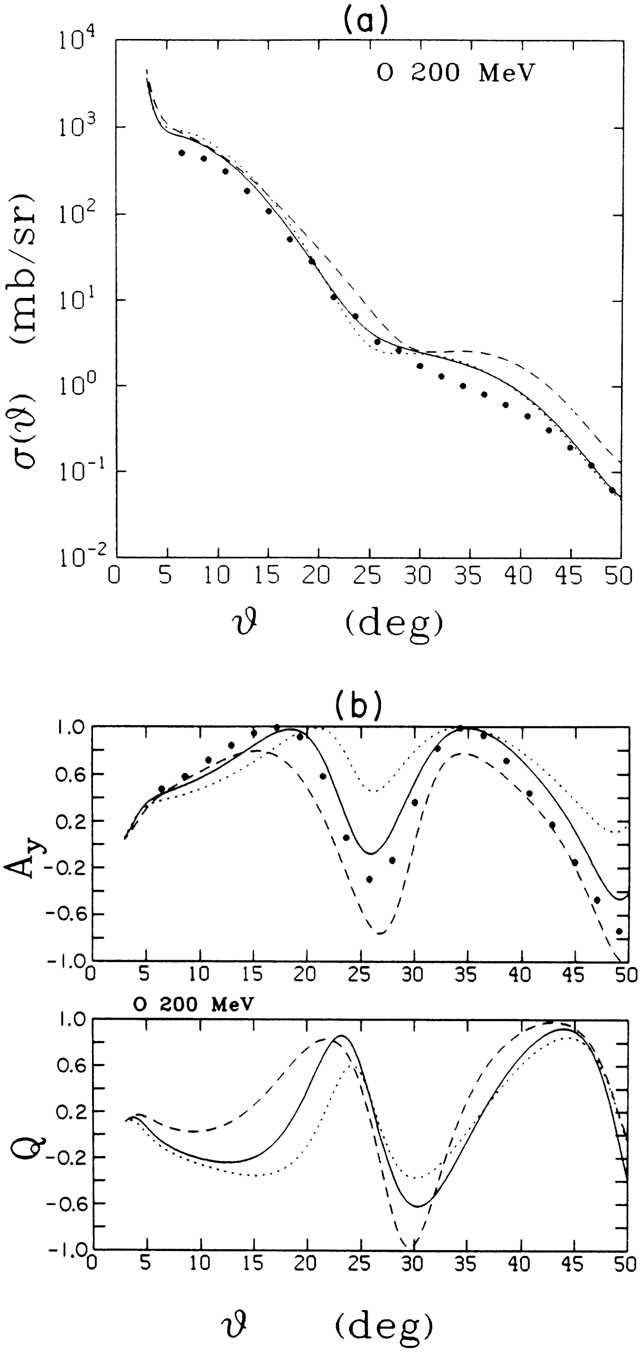

FIG. 18. The differential cross section, analyzing power (A_Y), and spin rotation function (Q) for 200 MeV protons scattering from ^{16}O. The solid line shows the IA2 result, the dashed line shows the IA1 result, and the dotted line shows the NRIA result. The data are from Ref. 32.

able data over the spectrum of energies and targets considered in this paper. Notably the IA2 description of the data is still an improvement over the NRIA result. As we show in a separate article, the inclusion of vacuum polarization corrections is capable of removing the discrepancy of the IA2 analysis with these data.[27] The IA1 result excels in fitting the A_Y data precisely through about 26 deg. For the whole range of Q data, the IA1 result is very good.

At 200 MeV the story is similar to that for ^{40}Ca, as may be seen in Fig. 15. The cross section calculations display too much oscillatory structure compared to the data.[28,29] The IA2 result reproduces the A_Y and Q data extremely well through about 27 deg, but then begins to fail. The IA1 result for A_Y fails to describe the minimum at about 17 deg, but is reasonably close to the data elsewhere. The NRIA result for A_Y describes that minimum, but does not do as well elsewhere. The three calculations of spin observable Q are quite different, and IA2 provides the best agreement with the data.

C. ^{16}O

At 800 MeV, again the IA1 , IA2 , and NRIA results reproduce the cross section data[30] comparably well as shown in Fig. 16. For A_Y, IA2 and IA1 results are quite similar through about 12 deg. The NRIA result misses the first minimum of A_Y, but after about 12 deg compares favorably with the data. All three calculations describe Q data well through about 12 deg and then they begin to fail, with NRIA providing perhaps the best reproduction of the data.

At 500 MeV there are smaller differences between the three impulse approximation results as shown in Fig. 17. Each provides a decent description of the data.[31] The NRIA result for the cross section has a minimum that is too deep but otherwise is as good as the others.

There is too much structure in the cross section at 200 MeV for all calculations, as seen in Fig. 18. The IA2 and NRIA results look very similar here, and both describe the data[32] better than does the IA1 result. As was the case for the other targets, the IA2 result for A_Y is very good here, while the NRIA result for A_Y is poor. The IA1 result misses the first minimum of A_Y, but succeeds elsewhere. Q data are not available, but they could prove interesting, as the three theoretical predictions have some significant differences.

V. COMPARISON OF IA2 WITH VARIATIONS OF IA1 BASED ON PSEUDOVECTOR πN COUPLING

For quite some time it has been recognized that the IA1 potential fails at low energy due to implicit inclusion of pseudoscalar πN coupling.[2] It is a fair question to ask whether just changing the pseudoscalar πN coupling to pseudovector coupling is an adequate repair as opposed to doing the full IA2 analysis. In principle the answer is no, because the virtual pair contributions to the optical potential are not well defined unless a complete set of NN amplitudes is used in the construction. However, results of Murdock and Horowitz for proton scattering[19] are quite good using a pseudovector covariant in place of the pseudoscalar covariant of IA1 and including Pauli-blocking corrections. This prescription does not eliminate the ambiguity in pair potentials because all NN amplitudes are fixed from positive-energy matrix elements, but it does cast the very large one-pion exchange contribution into a sensible form.

Several different methods exist for changing from pseudoscalar to pseudovector covariants. Two methods are

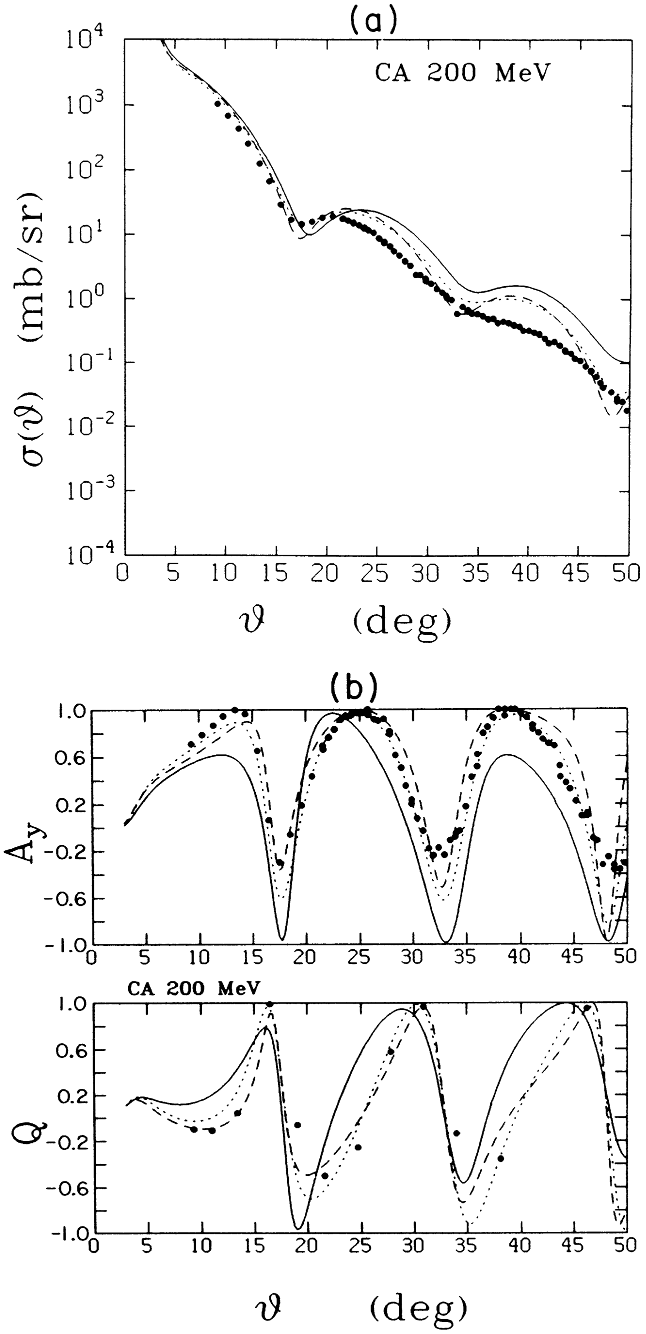

FIG. 19. The differential cross section, analyzing power (A_Y), and spin rotation function (Q) for 200 MeV protons scattering from ^{40}Ca. The solid line shows the IA1 result, the dashed line shows the IA1PV result, and the dotted line shows the IA1PV1 result.

described in Ref. 2 and we refer to them collectively as IA1PV1 since they produce essentially equivalent results. A more direct method is to subtract the pseudoscalar one-pion exchange amplitude from the *NN* amplitude of IA1 and then replace it with a pseudovector one-pion exchange amplitude. This procedure affects only the real parts of the amplitudes and it is called IA1PV. It gives more satisfactory results in comparison with the full IA2 analysis than the prescription of Ref. 2. For ^{40}Ca, we find that the two prescriptions, IA1PV and IA1PV1, yield comparable results as shown in Fig. 19. This figure shows the IA1 result (solid line), the IA1PV1 result

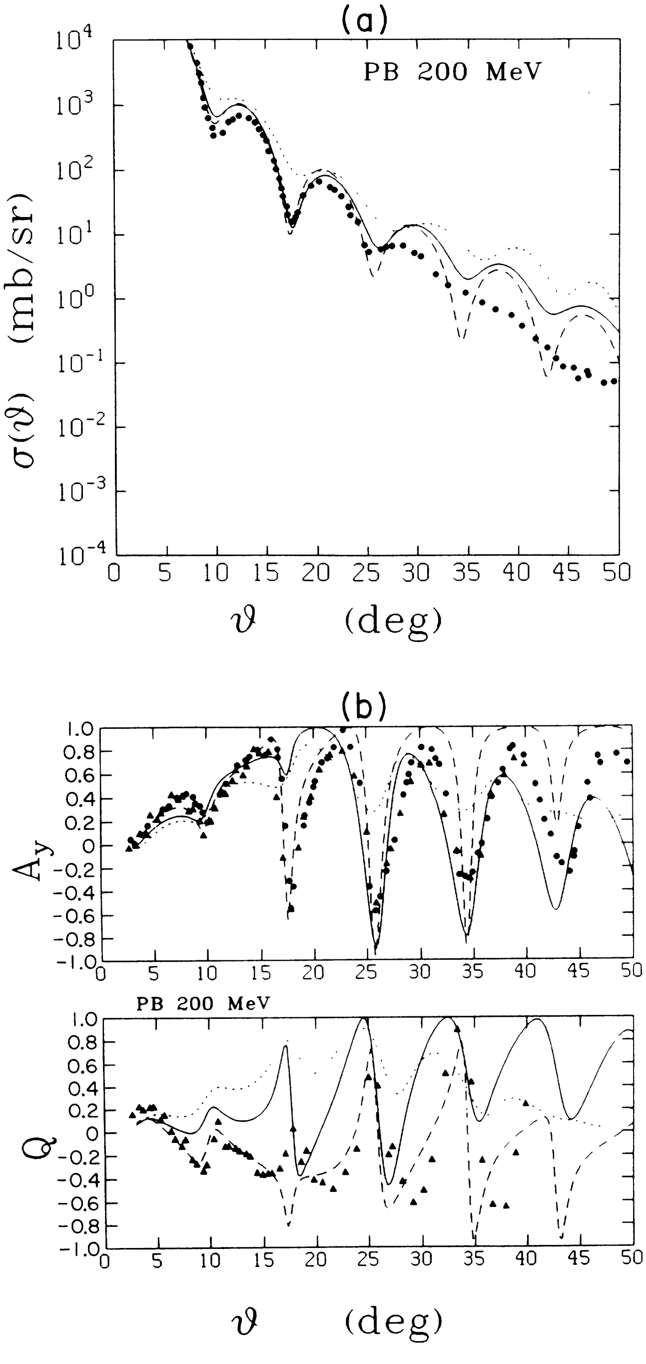

FIG. 20. The differential cross section, analyzing power (A_Y), and spin rotation function (Q) for 200 MeV protons scattering from ^{208}Pb. The solid line shows the IA1 result, the dashed line shows the IA1PV result, and the dotted line shows the IA1PV result.

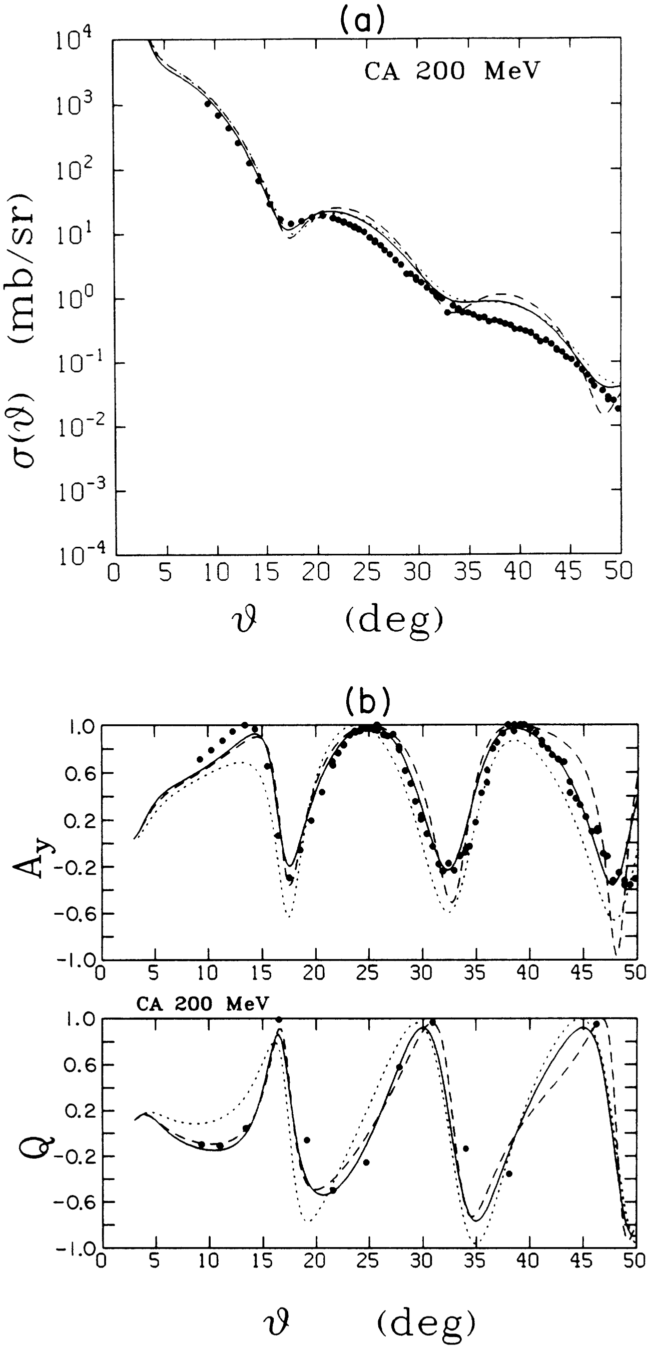

FIG. 21. The differential cross section, analyzing power (A_Y), and spin rotation function (Q) for 200 MeV protons scattering from ^{40}Ca. The solid line shows the IA2 result, the dashed line shows the IA1PV result, and the dotted line shows the Horowitz result (Ref. 33).

(dashed line), and the IA1PV result (dotted line) for calcium at 200 MeV. Both prescriptions for changing to pseudovector coupling improve upon the IA1 results, and we find that this is true at higher energies also. However, for ^{208}Pb, there is a surprise. As seen in Fig. 20, the IA1PV1 prescription fails to produce reasonable cross sections or spin observables. While for ^{40}Ca the pseudovector prescriptions produce similar results, for ^{208}Pb they differ greatly. This is caused by differences in imaginary parts of isovector amplitudes which average out in ^{40}Ca, but which are quite large for $N \neq Z$ nuclei such as lead. The IA1PV1 prescription does transform the real one-pion exchange interaction correctly, but it also changes the imaginary parts of some amplitudes. We find that it fails at all three energies for ^{208}Pb. This example shows that the ambiguity in changing from pseudoscalar to pseudovector coupling can be substantial.

Another prescription for implementing pseudovector coupling has been suggested by Horowitz.[33] Figure 21 compares the IA2 result (solid line), with the IA1PV prescription (dashed line) and the Horowitz prescription (dotted line) for ^{40}Ca at 200 MeV. There is considerable sensitivity of proton scattering observables to various ways of extending the NN amplitudes to the full Dirac space of two nucleons. Similar results are obtained for ^{208}Pb at 200 MeV.

VI. ROLE OF THE SMALL POTENTIALS

Compared to the $\tilde{S}$ and $\tilde{V}$ potentials, the $\tilde{T}$, $\tilde{S}_{LS}$, and $\tilde{V}_{LS}$ potential of Eq. (4) are quite small. Therefore one may question whether these potentials are really needed. For ^{40}Ca at 800 MeV, omission of either $\tilde{T}$, or both $\tilde{S}_{LS}$ and $\tilde{V}_{LS}$, causes the results for A_Y and Q to change dramatically, even though the cross section is essentially unchanged. This is shown in Fig. 22. If all three of the small potentials are omitted, there is a smaller effect. Thus some cancellation of the effects of the small potentials may be inferred at 800 MeV. At 500 and 200 MeV the corresponding changes are not as dramatic with respect to omitting $\tilde{T}$ or both $\tilde{S}_{LS}$ and $\tilde{V}_{LS}$, but omitting all three does make a considerable difference. Similar results are found for ^{16}O and ^{208}Pb targets.

Although Dirac potentials $\tilde{T}(r)$, $\tilde{S}_{LS}(r)$, and $\tilde{V}_{LS}(r)$ are each small in magnitude, they contribute significantly to the spin-orbit potential of the equivalent Schrödinger equation. Figure 23 shows that the equivalent Schrödinger spin-orbit potential for ^{40}Ca at 500 MeV is changed significantly by omission of these small potentials. However, we find that the equivalent central potential is virtually unchanged. Thus the small potentials, $\tilde{T}$, $\tilde{S}_{LS}$, and $\tilde{V}_{LS}$ of the generalized impulse approximation can be significant to the analysis of spin observables.

VII. SUMMARY AND OUTLOOK

Interesting results for proton-nucleus scattering have emerged from the Dirac approach based on relativistic NN amplitudes. The original form of the Dirac impulse approximation, called IA1, provides a direct connection of the large scalar and vector potentials to NN amplitudes. Moreover, successful descriptions of spin observables in proton scattering are obtained at energies above about 300 MeV. These features persist in the generalized

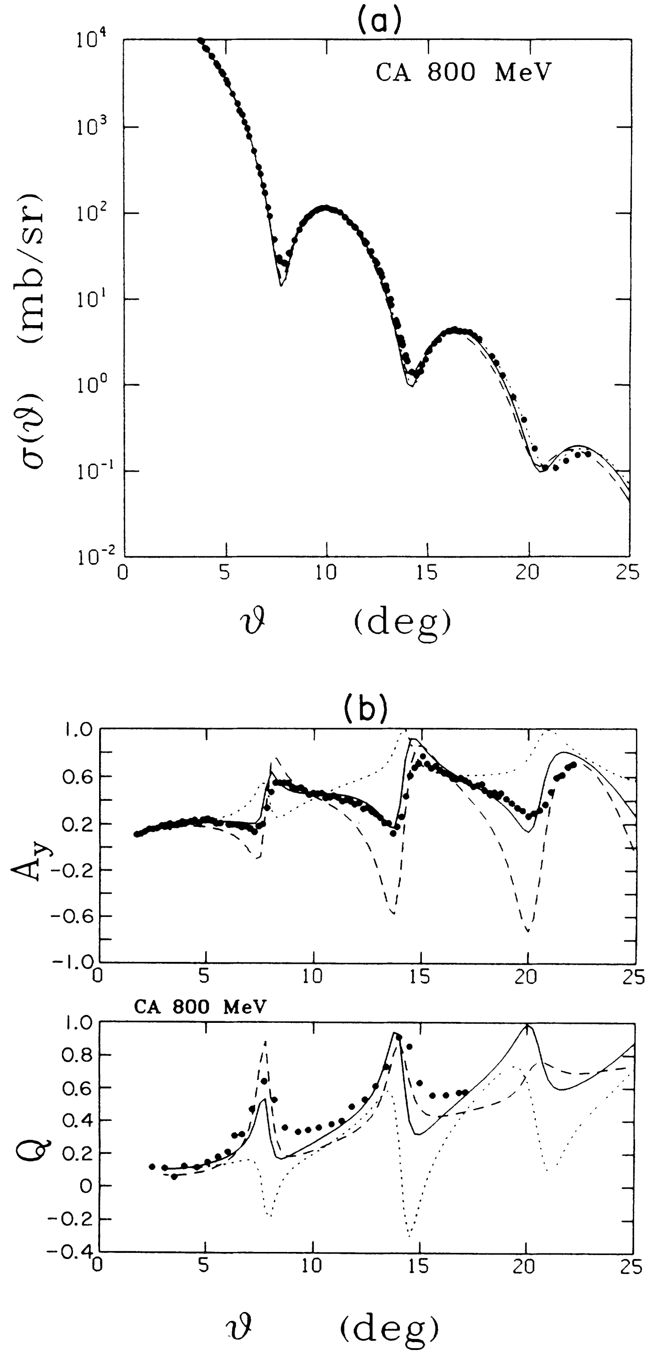

FIG. 22. The differential cross section, analyzing power (A_Y), and spin rotation function (Q) for 800 MeV protons scattering from ^{40}Ca. The solid line shows the IA2 result, the dashed line shows the IA2 result omitting both S_{LS} and V_{LS} potentials, and the dotted line shows the IA2 result omitting the T potential.

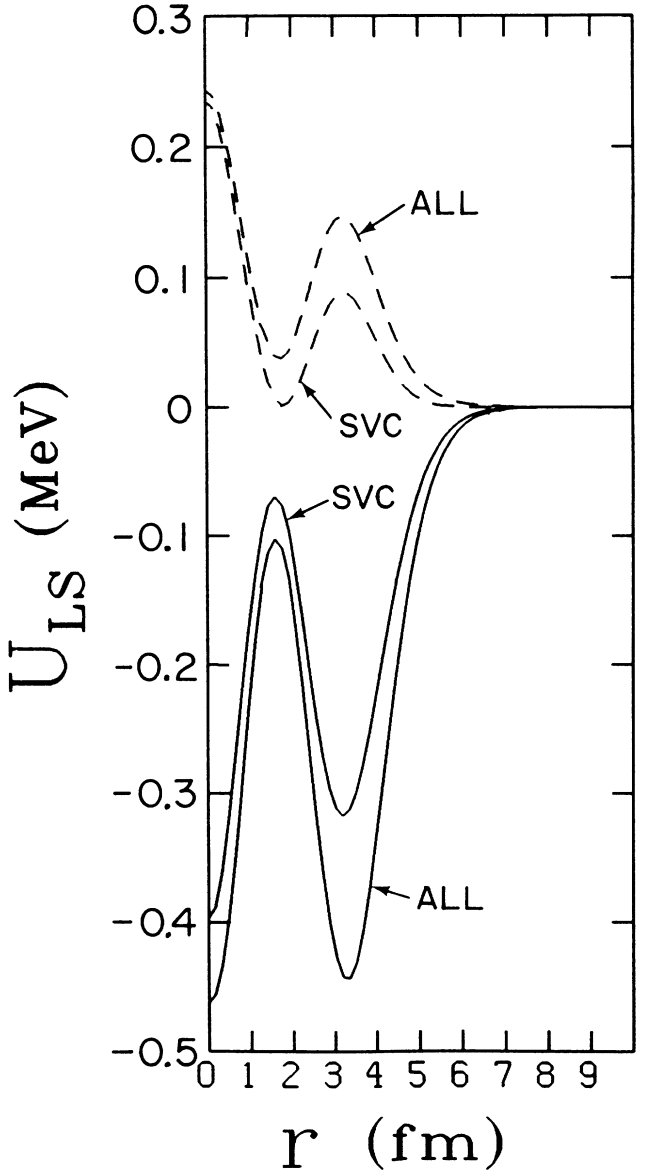

FIG. 23. The ^{40}Ca equivalent Schrödinger spin-orbit potential for 500 MeV including all Dirac potentials and including just the S, V, and C potentials

impulse approximation, called IA2, and they are brought under control within the context of meson-exchange models of the nuclear force. For several years the problem has been to establish dynamical control over the virtual-pair contributions which enter implicity when one solves the Dirac equation. As shown in Sec. II, the pair potentials remain large, about 25 meV, throughout the 200–800 MeV energy range, and this is in contrast to Pauli-blocking corrections to the NN interaction. IA2 achieves control over them by basing the Dirac optical potential on a complete set of NN amplitudes determined from a meson-exchange model of the nuclear force. Pseudovector πN coupling is incorporated consistently and vertex cutoffs are used to regulate high-momentum behavior. The. model used provides a qualitative description of the NN amplitudes over a broad energy region, and this constraint is adopted to avoid a large class of ambiguities (but not all ambiguity) in the construction of the Dirac optical potential from NN amplitudes. Prescriptions for incorporating pseudovector πN coupling in a simpler manner[2,33] produce significantly different results.

Overall, the generalized impulse approximation succeeds in describing a large body of proton scattering data using meson couplings determined from the analysis of NN scattering. Particularly at lower proton energies it provides significant improvement over the original impulse approximation. Most important, a dynamical basis for the virtual-pair contributions is established. IA2 unifies the analysis of proton optical potentials with the analysis of the NN interaction, and to a certain extent with the analysis of meson-exchange corrections, since these also are commonly calculated from a similar meson-exchange dynamics.

ACKNOWLEDGMENTS

The support of the U.S. Department of Energy under Grant No. DE-FG05-87ER-40322, and of the University of Maryland Computer Science Center is gratefully acknowledged. We thank Dr. L. Ray for supplying the matter densities of Refs. 20 and 21 in the form of a computer file.

APPENDIX

Equivalent Schrödinger central and spin-orbit potentials can be defined such that the scattering is the same based on the Dirac and Schrödinger equations. In general the equivalent Schrödinger potentials depend on r (radius), ℓ (orbital angular momentum), and E (energy). Consider the Dirac equation with a five-term optical potential of Eqs. (3) and (4) without the two electromagnetic terms. Expand $\psi(r)$ into partial waves using normalized spin-angular functions $\mathcal{Y}^{m}_{j\ell}(\hat{r})$.[34]

$$\psi=\sum_{j\ell m}\begin{Bmatrix} F^{\pm}_{j\ell}(r) \\ i\sigma_r G^{\pm}_{j\ell}(r)\end{Bmatrix}\mathcal{Y}^{m}_{j\ell}(\hat{r}) \; . \tag{A1}$$

Expand the Dirac equation into coupled equations for the upper- and lower-component wave functions, $F(r)$ and $G(r)$, as follows:

$$\{E-m-\tilde{S}(r)-\tilde{V}(r)+[\tilde{S}_{LS}(r)+\tilde{V}_{LS}(r)]\kappa\}F-\frac{dG}{dr}+\frac{\bar{\kappa}}{r}G-\tilde{T}(r)G=0 \; , \tag{A2}$$

$$-i\sigma\cdot\hat{r}\left\{\frac{dF}{dr}-\frac{\kappa}{r}F-\tilde{T}(r)F+[E+m+\tilde{S}(r)-\tilde{V}(r)]G+[\tilde{V}_{LS}(r)-\tilde{S}_{LS}(r)]\bar{\kappa}G\right\}=0\ . \tag{A3}$$

where

$$\kappa=j(j+1)-\ell(\ell+1)-\tfrac{3}{4}\ , \tag{A4}$$

$$\bar{\kappa}=j(j+1)-\bar{\ell}(\bar{\ell}+1)-\tfrac{3}{4}\ , \tag{A5}$$

and

$$\bar{\ell}=2j-\ell\ . \tag{A6}$$

We can rewrite these as

$$\left[\frac{d}{dr}-\frac{\bar{\kappa}}{r}+\tilde{T}\right]G=W(r,\kappa)F\ , \tag{A7}$$

$$\left[\frac{d}{dr}-\frac{\kappa}{r}-\tilde{T}\right]F=-Q(r,\bar{\kappa})G\ , \tag{A8}$$

where

$$W(r,\kappa)=E-m-\tilde{S}-\tilde{V}+[\tilde{S}_{LS}(r)+\tilde{V}_{LS}(r)]\kappa\ , \tag{A9}$$

$$Q(r,\bar{\kappa})=E+m+\tilde{S}-\tilde{V}+[\tilde{V}_{LS}(r)-\tilde{S}_{LS}(r)]\bar{\kappa}\ . \tag{A10}$$

Equation (A8) may be solved for the lower-component wave function, $G(r)$, and the result substituted into Eq. (A7) to obtain a nonlocal form of the Schrödinger equation.

$$\frac{d^2}{dr}F+\left[-\frac{1}{Q}\frac{dQ}{dr}+\frac{2}{r}\right]\frac{dF}{dr}+\left[\frac{1}{Q}\frac{dQ}{dr}\left(\frac{\kappa}{r}+\tilde{T}\right)-\frac{\ell(\ell+1)}{r^2}-\frac{d\tilde{T}}{dr}-\tilde{T}^2+\frac{\bar{\kappa}-\kappa}{r}\tilde{T}\right]F=-QWF\ . \tag{A11}$$

If we make the substitution $F(r)=r^{-1}Q^{1/2}\phi(r)$, then the term involving dF/dr is eliminated. Finally dividing by $r^{-1}Q^{1/2}$ produces a Schrödinger equation for ϕ,

$$\frac{d^2\phi}{dr}-\frac{\ell(\ell+1)}{r^2}\phi=-[k^2-(E+m)U]\phi\ , \tag{A12}$$

where $E^2-m^2=k^2$, and the Schrödinger potential U is given by

$$\begin{aligned}(E+m)U=&-[(E-m)(\tilde{S}-\tilde{V})-((E+m)(\tilde{S}+\tilde{V})-\tilde{S}^2+\tilde{V}^2]-[A(\tilde{S}_{LS}+\tilde{V}_{LS})\kappa+B(\tilde{V}_{LS}-\tilde{S}_{LS})\bar{\kappa}+(\tilde{V}^2_{LS}-\tilde{S}^2_{LS})\kappa\bar{\kappa}]\\&-\left[\frac{1}{2}\frac{1}{Q}\frac{d^2Q}{dr^2}-\frac{3}{4}\left(\frac{1}{Q}\frac{dQ}{dr}\right)^2+\left(\frac{1}{Q}\frac{dQ}{dr}\right)\left(\frac{\kappa+1}{r}\right)\right]-\left(\frac{1}{Q}\frac{dQ}{dr}\tilde{T}-\frac{d\tilde{T}}{dr}-\tilde{T}^2+\frac{\bar{\kappa}-\kappa}{r}\tilde{T}\right)\ ,\end{aligned} \tag{A13}$$

where

$$A=E+m+\tilde{S}-\tilde{V} \tag{A14}$$

and

$$B=E-m-\tilde{S}-\tilde{V}\ . \tag{A15}$$

In order to split U into central and spin-orbit terms, define

$$U_+ \equiv U(\kappa=\ell, \bar{\kappa}=-\ell-2)$$

and

$$U_- \equiv U(\kappa=-\ell-1, \bar{\kappa}=\ell-1) \, .$$

Then the central potential is

$$U_c = \frac{\ell+1}{2\ell+1} U_+ + \frac{\ell}{2\ell+1} U_- \tag{A16}$$

and the spin-orbit potential is

$$U_{LS} = \frac{U_+ - U_-}{2\ell+1} \, . \tag{A17}$$

Numerical results for $\ell=0$ states are given in Sec. II.

---

[1] J. A. Tjon and S. J. Wallace, Phys. Rev. Lett. **54**, 1357 (1985).
[2] J. A. Tjon and S. J. Wallace, Phys. Rev. C **32**, 267 (1985).
[3] J. A. Tjon and S. J. Wallace, Phys. Rev. C **36**, 1085 (1987).
[4] J. A. Tjon and S. J. Wallace, Phys. Rev. C **32**, 1667 (1985).
[5] J. A. Tjon and S. J. Wallace, Phys. Rev. C **35**, 280 (1987).
[6] J. A. McNeil, J. R. Shepard, and S. J. Wallace, Phys. Rev. Lett. **50**, 1439 (1983); J. R. Shepard, J. A. McNeil, and S. J. Wallace, *ibid.* **50**, 1444 (1983).
[7] B. C. Clark, S. Hama, R. L. Mercer, L. Ray, and B. D. Serot, Phys. Rev. Lett. **50**, 1644 (1983).
[8] J. A. McNeil, L. Ray, and S. J. Wallace, Phys. Rev. C **27**, 2123 (1983).
[9] B. C. Clark, S. Hama, R. L. Mercer, L. Ray, G. W. Hoffmann, and B. D. Serot, Phys. Rev. C **28**, 1421 (1983).
[10] L. Ray and G. W. Hoffmann, Phys. Rev. C **31**, 538 (1985).
[11] M. V. Hynes, A. Picklesimer, P. C. Tandy, and R. M. Thaler, Phys. Rev. Lett. **52**, 978 (1984).
[12] M. V. Hynes, A. Picklesimer, P. C. Tandy, and R. M. Thaler, Phys. Rev. C **31**, 1435 (1985).
[13] E. E. van Faassen and J. A. Tjon, Phys. Rev. C **28**, 2354 (1984).
[14] E. E. van Faassen and J. A. Tjon, Phys. Rev. C **30**, 285 (1984).
[15] E. E. van Faassen, Ph.D. thesis, University of Utrecht, 1985 (unpublished).
[16] C. J. Horowitz and B. D. Serot, Nucl. Phys. **A368**, 503 (1981).
[17] R. A. Arndt, L. D. Roper, R. A. Bryan, R. B. Clark, B. J. VerWest, and P. Signell, Phys. Rev. D **28**, 97 (1983).
[18] A. K. Kerman, H. McManus, and R. M. Thaler, Ann. Phys. (N.Y.) **8**, 551 (1959).
[19] D. P. Murdock and C. J. Horowitz, Phys. Rev. C **35**, 1442 (1987).
[20] L. Ray, Phys. Rev. C **19**, 1855 (1979); see also Ref. 10.
[21] J. DeChargé and D. Gogny, Phys. Rev. C **21**, 1568 (1980); J. DeChargé, M. Girod, D. Gogny, and B. Grammaticos, Nucl. Phys. **A358**, 203c (1981).
[22] P. Schwandt, private communication.
[23] E. J. Stephenson, J. Phys. Soc. Jpn. (Suppl.) **55**, 316 (1985).
[24] G. W. Hoffmann *et al.*, Phys. Rev. Lett. **47**, 1436 (1981).
[25] A. Rahbar *et al.*, Phys. Rev. Lett. **47**, 1811 (1981).
[26] G. W. Hoffmann *et al.*, Phys. Rev. C **21**, 1488 (1980); **24**, 541 (1981); R. W. Fergerson *et al.*, Phys. Rev. C **33**, 239 (1986).
[27] N. Ottenstein, S. J. Wallace, and J. A. Tjon, Phys. Lett. B **197**, 493 (1987).
[28] D. A. Hutcheon *et al.*, in *Polarization Phenomena in Nuclear Physics-1980 (Fifth International Symposium, Santa Fe)*, Proceedings of Fifth International Symposium on Polarization Phenomena in Nuclear Physics, AIP Conf. Proc. No. 69, edited by G. G. Ohlson, R. E. Brown, N. Jarmie, W. W. McNaughton, and G. M. Hale (AIP, New York, 1981).
[29] M. Ji, M. S. thesis, Simon Fraser University, 1987 (unpublished).
[30] G. S. Adams *et al.*, Phys. Rev. Lett. **43**, 421 (1979).
[31] M. V. Hynes and B. Aas, Los Alamos National Laboratory LA-9709-PR, 1982.
[32] C. W. Glover *et al.*, Phys. Rev. C **31**, 1 (1985).
[33] C. J. Horowitz, Phys. Rev. C **31**, 1340 (1985).
[34] J. J. Sakurai, *Advanced Quantum Mechanics* (Addison-Wesley, Reading, Mass., 1967), p. 124.